Compressive Sensing for Interferometric Inverse Synthetic Aperture Radar Applications

A. Bacci*†, D. Staglianò*†, E. Giusti†, S. Tomei*†, F. Berizzi*† and M. Martorella*†

*Department of Information Engineering, University of Pisa, Italy

† CNIT Radar and Surveillance System (RaSS) National Laboratory, Pisa, Italy

Email:alessio.bacci@for.unipi.it

Abstract

The applicability of Interferometric Inverse Synthetic Aperture radar techniques to images reconstructed via Compressive Based algorithms is investigated. Specifically, the 3D reconstruction algorithm is applied after exploiting CS for data compression and image reconstruction. The InISAR signal model is derived and formalized in a CS framework. A comparison between conventional CS reconstruction and global sparsity constrained reconstruction techniques is performed for different compression rate and different Signal to Noise Ratio conditions. Performance on the 2D and 3D reconstruction are evaluated. Results obtained on real data acquired during the NATO-Set 196 trial are shown.

I. INTRODUCTION (TUTTI)

Inverse Synthetic Aperture Radar (ISAR) has been studied for more than three decades and several demonstrations have proven its effectiveness in forming electromagnetic images of non-cooperative moving targets [1], [30]. The conventional ISAR imaging approach produces 2D images of targets by projecting the reflectivity function onto the Image Projection Plane (IPP) [1], [29], [20]. This means that the same target may produce very different projections and then appear very different as the IPP changes. As a consequence, Automatic Target Recognition (ATR) can be a challenging task when ISAR images are used as input.

Three-dimensional (3D) ISAR imaging can therefore be seen as a logical solution to such a problem as it produces 3D target reconstructions, and therefore avoids the target's projection onto image planes. 3D ISAR imaging has been a subject of research for many years. In [14], a 3D imaging algorithm based on a tomographic approach that extends the synthetic aperture both along the azimuth and the elevation

was developed. A key factor in achieving accurate 3D images is precise control over the radar LoS (Line of Sight) incident angle. Such accuracy can be achieved in controlled experiments, such as in the case of turntables [27]. The use of ISAR image snapshots to form 3D images of fast rotating objects when the spinning velocity is much higher than the precession velocity has been proposed in [13]. The effectiveness of this method was proven in the case of ballistic missile 3D imaging. Another way of forming 3D ISAR images was proposed in [16], [15], [26], where a sequence of ISAR images is used to track scattering center range histories. The 3D location of such scatterers is then estimated by using such tracks and by exploiting geometrical constraints induced by rigid bodies. All the above mentioned methods rely on long observation time and their performances strongly depend on the target's motion. Other techniques to obtain 3D ISAR images based on the use of multi-channel sensors and interferometry have been proposed [31], [12], [10], [6]. It should be pointed that, in these cases, the 3D target reconstruction is not a full 3D image, as the scatterer's elevation with respect to the IPP is obtained as a result of an estimation problem and not as an output of an imaging algorithm. Nevertheless, a direct advantage of using such techniques is that no a priori knowledge of the target's rotational motion is required and their effectiveness does not depend on such a motion. The author of [16], [15] proposed a novel algorithm for producing 3D ISAR images of targets by combining ISAR image sequences and interferometry.

In this paper, the problem of 3D target reconstruction has been addressed by using the technique described [21]. The proposed algorithm introduces a new estimation problem, which involves the joint estimation of the target's effective rotation vector (both modulus and phase) and the height of the scattering centres by using a dual interferometric ISAR system. The estimation of the effective rotation vector allows the ISAR image plane to be estimated and the height of the dominant scatterers to be calculated. It is worth pointing out that such a technique requires the computation of at least three 2D ISAR images of the target of interest leading to a large amount of data to be stored and processed. In order to reduce this amount of data, Compressive Sensing (CS) can be applied to each 2D ISAR image. In fact, recent results in signal processing have demonstrated the ability of CS to reconstruct a sparse or compressible signal from a limited number of measurements with a high probability by solving an optimization problem [5]. Such a technique was proposed for data storage reduction in medical imaging [19] and radar imaging applications [3] among others. In the last few years the interest of the radar scientific community in the application of CS has raised and different applications have been investigated such as Synthetic Aperture Radar (SAR) imaging and ISAR [24], ground penetrating radars [11], Multiple Input Multiple Output (MIMO) radar [32][2] and 3D ISAR imaging [23]. The applicability of CS is based on the fact that the ISAR image is a sparse representation of the ISAR data as the number of dominant scatterers is usually much smaller

than the number of pixels in the image [33]. In this work a method to obtain 3D InISAR (Interferometric ISAR) reconstruction by applying CS to reconstruct 2D ISAR images from compressed data is proposed. It is worth pointing out that, although the capability of CS to reconstruct good quality images amplitude is widely treated in literature [33], [22], its capability in the recovery of the image phase is still an open research field. A first attempt in assessing the reconstruction performance for both amplitude and phase is in [9]. Specifically, in the present work, the performance assessment will be evaluated on the estimation of the effective rotation vector which is fundamental for the 3D reconstruction. Different reconstruction methods will introduced and compared by using a measured dataset. The paper is organized as follows. In Sect. II the 3D InISAR signal model and reconstruction method will be presented in a CS framework. In particular, three different CS reconstruction techniques will be introduced. In Sect. III results on real data will be shown. A performance analysis will be conducted and some conclusion will be drawn in Sect. IV.

II. 3D-InISAR in a CS framework
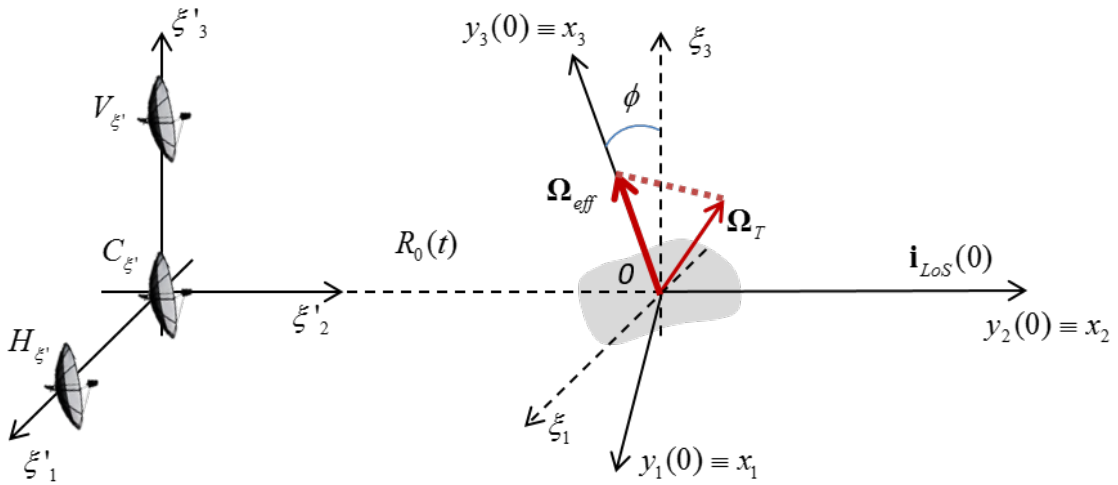
A. Signal Model

Figure 1. ISAR system geometry

The system described in Figure 1 consists of three antennas arranged in an L-shape configuration with vertical baseline d_V and horizontal baseline d_H. Having to deal with three reference systems, we will denote points in the 3D space by using a subscript according to the specific reference system coordinates, e.g. $\mathbf{C}_\xi$ and $\mathbf{C}_y$ are the same point expressed with the reference system coordinates T_ξ and T_y respectively.

The point $\mathbf{C}_{\xi'}$ corresponds with the origin of the reference system $T_{\xi'}$, that is the antenna array phase center. The antennas located at points $\mathbf{V}_{\xi'}$ and $\mathbf{H}_{\xi'}$ lie on the ξ'_3- and ξ'_1- axis respectively. The reference system $T_{\xi'}$ is embedded in the radar system while T_x is the time-varying reference system embedded in the target and T_y is coincident with T_x at time $t = 0$. The reference system T_ξ corresponds to $T_{\xi'}$ but it is centred on the target. For simplicity of representation, let the three antennas be considered both transmitting and receiving. Such a configuration would require the use of orthogonal waveforms in order to separate the three channels. However, equal effectiveness could be achieved by considering the use of one transmitter and a certain number of co-located receivers.

Finally, the target is described as a rigid body fixed with respect to T_y, composed of K point-like scatterers with complex amplitude ρ_k and with position $\mathbf{y} = [y_1, y_2, y_3]$ at time $t = 0$ for the generic k^{th} scatterer.

Let $s_T(t)$ be the analytical signal associated with a wideband transmitted pulse. Under the hypothesis of small aspect angle variations, the interactions among the scatterers can be neglected. As a consequence, the discrete baseband signal at the output of the matched filter at the ith receiver associated with a single scatterer, after motion compensation, is given by:

$$S_R^{(i)}(n\Delta f, mT_R) \doteq S_R^{(i)}(n,m) = \rho^{(i)} \exp\left\{-j\frac{4\pi}{\lambda}\left[\mathbf{y} \cdot \mathbf{i}_{LoS_y}^{(i)}(m)\right]\right\} W(n,m) \tag{1}$$

where

$$W(m,n) = (u(n) - u(n-N)) \cdot (u(m) - u(m-M)) \tag{2}$$

and $n = -\frac{N}{2}, ..., \frac{N}{2} - 1$ is the frequency (range) index, Δf the frequency sampling interval, $m = -\frac{M}{2}, ..., \frac{M}{2} - 1$ is the slow time index, T_R is the Pulse Repetition Interval (PRI), $\mathbf{i}_{LoS_y}^{(i)}$ is the LoS unit vector expressed with respect to T_y and the function $u(x) = 1$ for $x \geq 0$. Due to the very limited baselines, the reflectivity functions $\rho^{(i)}$ at each channel can be considered the same, i.e. $\rho^{(i)} = \rho$. In the following Δf and T_R will be omitted to simplify the notation.

As shown in [21] it can be demonstrated that

$$\mathbf{y} \cdot \mathbf{i}_{LoS_y}^{(i)}(m) = K_0^{(i)} + K_1^{(i)} m \tag{3}$$

where

$$
\begin{bmatrix} K_0^V + K_1^V m \\ K_0^C + K_1^C m \\ K_0^H + K_1^H m \end{bmatrix} =
$$

$$
= \begin{bmatrix} y_2 + c_2 m - \frac{d_V}{R_0}\left[(y_1 + c_1 m)\sin\phi + (y_3 + c_3 m)\cos\phi\right] \\ y_2 + c_2 m \\ y_2 + c_2 m + \frac{d_H}{R_0}\left[(y_3 + c_3 m)\sin\phi - (y_1 + c_1 m)\cos\phi\right] \end{bmatrix}
$$

(4)

where the terms c_1, c_2 and c_3 are the components of the vector $\mathbf{c} = \mathbf{\Omega_T} \times \mathbf{y}$ and ϕ is the angle describing the rotation of the reference system T_y with respect to T_ξ and R_0 is the modulus of the LoS unit vector which locates the position of the focusing point O.

The ISAR image at the ith receiver can be obtained via a 2D-DFT of the received signal [4] and can be expressed as follows

$$
I^{(i)}(n_\tau, m_\nu) \doteq I^{(i)}(n_\tau \Delta\tau, m_\nu \Delta\nu) =
$$

$$
BT_{obs}\rho e^{j2\pi f_0\left(n_\tau - \frac{2}{c}K_0^{(i)}\right)}\text{sinc}\left[T_{obs}\left(m_\nu + \frac{2f_0}{c}K_1^{(i)}\right)\right]\text{sinc}\left[B\left(n_\tau - \frac{2}{c}K_0^{(i)}\right)\right]
$$

(5)

where n_τ and m_ν denotes the delay time and Doppler frequency indexes respectively, while $\Delta\tau$ and $\Delta\nu$ are the delay time and Doppler frequency sampling interval respectively and will be omitted to simplify the notation in the following.

B. CS based modelling and reconstruction

As is evident from Eq.(5) the relationship between the ISAR image, $I^{(i)}(n_\tau, m_\nu)$ and the ISAR signal $S^{(i)}(n, m)$ is given by a two dimensional Fourier Transformation. In fact, the ISAR image is a representation of the ISAR signal in the 2D Fourier basis. This relationship can be expressed in a matricial form as

$$
\mathbf{S}^{(i)} = \mathbf{\Psi}_R \mathbf{I}^{(i)} \mathbf{\Psi}_D^T
$$

(6)

where $\mathbf{S}^{(i)} \in C^{N \times M}$ is the signal matrix relative to the ith channel, $\boldsymbol{I}^{(i)} \in C^{N_\tau \times M_\nu}$ $\mathbf{\Psi}_D \in C^{M \times M_\nu}$ and $\mathbf{\Psi}_R \in C^{N \times N_\tau}$ are the Fourier dictionaries which define the ISAR image domain. The reduction of size of the data can be now performed by applying a sensing operation along the two dimension as

$$
\mathbf{Y}^{(i)} = \mathbf{\Phi}_R \mathbf{S}^{(i)} \mathbf{\Phi}_D^T = \mathbf{\Phi}_R \mathbf{\Psi}_R \mathbf{I}^{(i)} \mathbf{\Psi}_D^T \mathbf{\Phi}_D^T
$$

(7)

where $\mathbf{\Phi}_R \in C^{N' \times N}$ and $\mathbf{\Phi}_D \in C^{M' \times M}$ are the sensing matrices with $N' < N$ and $M' < M$ and $\mathbf{Y}^{(i)}$ is the measurement matrix associated with the ith channel. It is worth pointing out that, in order for the

image to be reconstructed, the incoherence between the dictionaries and the sensing matrices, i.e., the Restricted Isometry Property (RIP)[7], must hold true. It has been demonstrated in [34] that incomplete Fourier matrices satisfy the RIP property so that Eq.(7) becomes

$$\mathbf{Y}^{(i)} = \boldsymbol{\Theta}_R \mathbf{I}^{(i)} \boldsymbol{\Theta}_D^T \tag{8}$$

where $\boldsymbol{\Theta}_R \in C^{N' \times N_\tau}$ and $\boldsymbol{\Theta}_D \in C^{M' \times M_\nu}$ are the incomplete matrices obtained by selecting N' and M' rows from the complete Fourier matrices $\boldsymbol{\Psi}_R$ and $\boldsymbol{\Psi}_D$. It is worth highlighting that the dependency on the channel index i of the sensing matrices has been omitted to simplify the notation, but the sensing operation can be different on each received signal. According to the CS framework an estimate of the ISAR image $\mathbf{I}^{(i)}$ can be obtained by solving the following minimization problem

$$\hat{\mathbf{I}}^{(i)} = \min_{\mathbf{I}^{(i)}} \|\mathbf{I}^{(i)}\|_{\ell_0} \quad s.t. \quad \|\mathbf{Y}^{(i)} - \boldsymbol{\Theta}_R \mathbf{I}^{(i)} \boldsymbol{\Theta}_D^T\|_F^2 \leq \epsilon \tag{9}$$

where ϵ is a small constant that depends on the noise level, $\|\cdot\|_{\ell_0}$ denotes the ℓ_0 norm and $\|\cdot\|_F$ is the Frobenius norm. In [8], a two dimensional smoothed ℓ_0 norm (2D-SL0) was proposed, which deals with two dimensional quantities and avoids the vectorization and Kronecker products that increases of the size of matrices leading to a more severe computational effort. The 2D-SL0 is based on the approximation of the ℓ_0 norm as follows

$$\| \mathbf{I}^{(i)} \|_{\ell_0} \approx N_\tau M_\nu - \sum_{n=0}^{N_\tau-1} \sum_{m=0}^{M_\nu-1} \exp\left\{-\frac{|\mathbf{I}^{(i)}|^2}{2\delta^2}\right\} \quad \text{when } \delta \to 0 \tag{10}$$

Then, a projective steepest descent optimal approach can be used to find the minimum value of $\| \mathbf{I}^{(i)} \|_{\ell_0}$. By observing Eq.(9) it is evident that the reconstruction is performed on each channel separately without considering the strong correlation that holds among the signals measured by the different receivers. In particular, all the ISAR images share the same sparsity support, that means that the scattering centers are located on the same positions in all the images. Considering this characteristic, the minimization problem can be formulated by considering a global sparsity measure, which avoids the issue related to non-aligned scatterers among the images reconstructed at different channels that may arise when Eq.(9) is applied. Two formulations of the global sparsity constraint can be found in [25] and are expressed as

$$\| \mathbf{I}_s \|_{\ell_0} = \| \sum_i \mathbf{I}^{(i)} \|_{\ell_0} \tag{11}$$

$$\| \mathbf{I}_m \|_{\ell_0} = \| \max_i \{\mathbf{I}^{(i)}\} \|_{\ell_0} \tag{12}$$

where $\| \max_i \{\mathbf{I}^{(i)}\} \|_{\ell_0}$ computes the max for each element matrix along i This two formulations of global sparsity will be denoted as global sparsity sum ($\|\mathbf{I}_s\|_{\ell_0}$) and global sparsity max ($\|\mathbf{I}_m\|_{\ell_0}$) in the following.
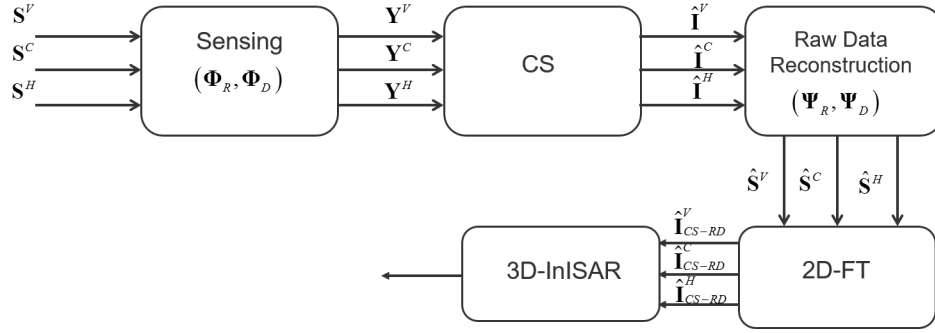
Figure 2. CS-RD Functional Blocks

Specifically, in Eq.(11) the common image support is obtained considering the sum of the three images while in Eq.(12) the sparsity support is obtained considering the maximum value, pixel by pixel, among the three images. Considering the global sparsity, the problem of non-aligned scattering centers among the reconstructed ISAR images is solved leading to a better 3D reconstruction.

The minimization problem considering the global sparsity is expressed as

$$\hat{\mathbf{I}}^{(i)} = \min_{\mathbf{I}^{(i)}} \|\mathbf{I}_{s/m}\|_{\ell_0} \quad s.t. \quad \left\{ \begin{array}{l} \|\mathbf{Y}^{(V)} - \mathbf{\Theta}_R \mathbf{I}^{(V)} \mathbf{\Theta}_D^T\|_F^2 \leq \epsilon \\ \|\mathbf{Y}^{(C)} - \mathbf{\Theta}_R \mathbf{I}^{(C)} \mathbf{\Theta}_D^T\|_F^2 \leq \epsilon \\ \|\mathbf{Y}^{(H)} - \mathbf{\Theta}_R \mathbf{I}^{(H)} \mathbf{\Theta}_D^T\|_F^2 \leq \epsilon \end{array} \right\} \tag{13}$$

where $\mathbf{I}_{s/m}$ denotes either the global sparsity sum or the global sparsity max according to the definition used. It is worth pointing out that the ISAR images at the output of the reconstruction toolbox are different from the images obtained with the Fourier based approach. In order to compare the images obtained from compressed data with the ones obtained with the full data the Compressive Sensing based Range Doppler (CS-RD) approach [28] will be considered. The $CS - RD$ block diagram is shown in Fig.2 for the sake of clarity.

C. 3D reconstruction

According to [21], the 3D reconstruction of the target is performed by the joint estimation of the modulus of the effective rotation vector Ω_{eff} and its direction expressed as the angle ϕ with respect to a reference system embedded on the target. These estimates depend on the phase differences between the received signals from the antennas along the vertical and horizontal baselines.

The phase differences can be computed by exploiting the received signals (in particular the ISAR

images) as follows:

$$\triangle\theta_V = \angle\left(I^V(n_\tau, m_\nu) \cdot I^{C^*}(n_\tau, m_\nu)\right) \tag{14}$$

$$\triangle\theta_H = \angle\left(I^H(n_\tau, m_\nu) \cdot I^{C^*}(n_\tau, m_\nu)\right) \tag{15}$$

where * denotes the complex conjugate.

After some mathematical manipulations (described in [21]) the vector of the coordinates of the target's scatterer $\mathbf{y}$ can be expressed as a function of the phase differences $\triangle\theta_V$, $\triangle\theta_H$ and the angle ϕ. In particular, y_3 represents the height of the scatterer with respect to the image plane and can be expressed as follows:

$$y_3 = \frac{c}{4\pi f_0} R_0 \left(\frac{\triangle\theta_V}{d_V} \cdot \cos\phi - \frac{\triangle\theta_H}{d_H} \cdot \sin\phi\right) \tag{16}$$

where c is the light speed in a vacuum and f_0 is the central frequency. From the Eq.(16), the heights of the scatterers can be calculated.

The Doppler component for each scatterer can be exploited in order to estimate the angle ϕ. After some algebra (described in [21]), Eq.(17) is obtained:

$$\nu_C = -\frac{2f_0}{c}K_1^C = -\frac{R_0\Omega_{eff}}{2\pi}\left(\frac{\triangle\theta_H}{d_H}\cos\phi + \frac{\triangle\theta_V}{d_V} \cdot \sin\phi\right) \tag{17}$$

where ν_C is the Doppler component for the scatterer under test for the C channel.

Consequently, Eq.(17) can be rewritten by considering only the contribution of the kth scatterer as follows:

$$Z_k = aY_k + bX_k \tag{18}$$

where $Z = \nu_C$, $Y = -\frac{R_0}{2\pi d_H} \cdot \triangle\theta_H$, $X = -\frac{R_0}{2\pi d_V} \cdot \triangle\theta_V$, $a = \Omega_{eff} \cdot \cos\phi$ and $b = \Omega_{eff} \cdot \sin\phi$.

Then, the estimates of Ω_{eff} and ϕ can be calculated by estimating a and b. This can be done by minimizing the functional:

$$\Upsilon(a,b) = \sum_{k=1}^{K_C} [Z_k - (aY_k + bX_k)]^2 \tag{19}$$

where K_C is the number of extracted scatterers by the MC-CLEAN technique [21]. Finally, the estimation of Ω_{eff} and ϕ can be derived from the estimates $\tilde{a}$ and $\tilde{b}$ as described below:

$$\begin{aligned} \hat{\Omega}_{eff} &= \sqrt{\tilde{a}^2 + \tilde{b}^2} \\ \hat{\phi} &= arctan\left(\frac{\tilde{b}}{\tilde{a}}\right) \end{aligned} \tag{20}$$

TX power	up to 33 dBm	Operative Frequency	10.55 ÷ 10.85 GHz
Chirp rate	up to 1.5 THz/s	Dynamic Range	-132 ÷ -38 dBm
Noise figure	4.2 dB	SFDR	65 dBc
System losses	8 dB	Receiver Gain	29 dB
Sampling freq.	12.5 MHz	ADC Resolution	14 bit

Table I

RADAR TRANSCEIVER SPECIFICATIONS

III. RESULTS ON REAL DATA

In this section the performance evaluation will be performed. Specifically, after introducing the dataset, the performance in terms of 2D ISAR image reconstruction in two different condition of Signal to Noise Ratio (SNR) and 3D reconstruction will be evaluated.

A. Dataset Description

An X-band interferometric ground-based Linear Frequency Modulated Continuous Wave (LFMCW) radar, namely PIRAD, has been used for collecting data in a real scenario. PIRAD is a multi-channel ground-based radar prototype designed and built within the Department of Information Engineering, University of Pisa [18], [17]. A picture of such a system is shown in Figure 3. PIRAD has been designed for the monitoring of ship traffic in harbour in all day/all weather conditions. The specifications of the PIRAD transceiver are summarized in Table I.

The antenna system consists of one transmitting and three receiving elements arranged in an L-shaped frame. An X-band Fabry-Perot resonator technology was adopted in order to realize compact and efficient horizontally polarized antennas. The developed antennas are characterized by the total absence of side lobes on the azimuth plane.

The experiment involved several non-cooperative vessels. The trial was carried out in October 2014 from the Institute "G. Vallauri" in the Italian Navy Base in occasion of NATO-SET 196 Joint Trials. PIRAD was aiming at the sea region in front of the site. The acquisition parameters are listed in Table II. Two vessels were moving during the acquisition and one sailing ship was stationary. The target that has been taken into account is shown in Fig. 4 (b) and its brief description is in Table III.

It should be pointed out that for a problem at the RF cable linking the central receiver (C), the data from that channel present a lower SNR which cannot be fixed it in post-processing (see Fig.5).
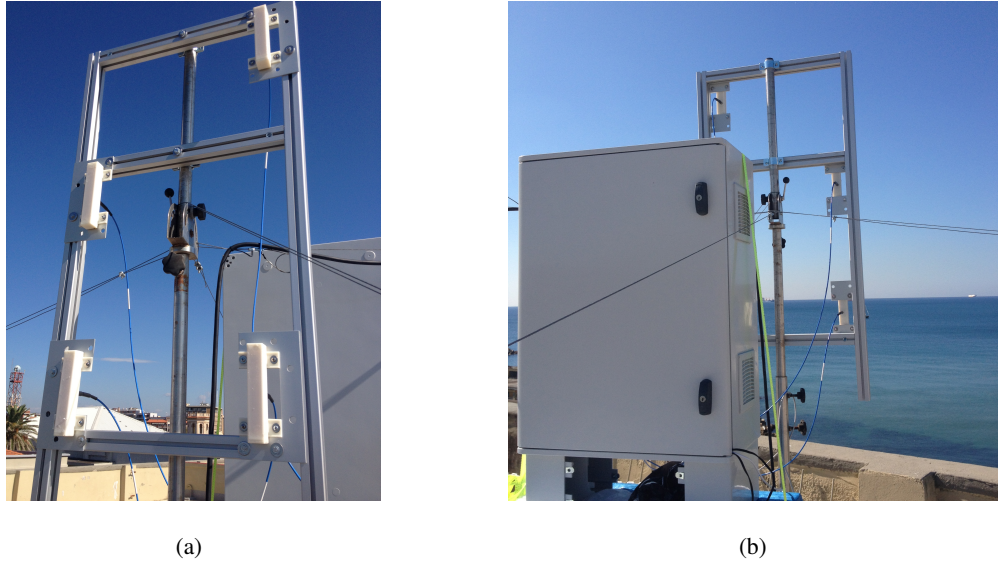
<div align="center">(a)</div>

<div align="center">(b)</div>

Figure 3. PIRAD system: (a) frame of the antennas; (b) cabinet and frame installed on a lifting structure

TX power	33 dBm
Bandwidth	300 MHz
PRF	1000 Hz
T_{obs}	1 s
Range resol.	0.5 m
Baselines	H: 0.41 m
	V: 0.47 m

<div align="center">Table II</div>

<div align="center">PIRAD'S ACQUISITION PARAMETER</div>

<div align="center">(a)</div>

<div align="center">(b)</div>
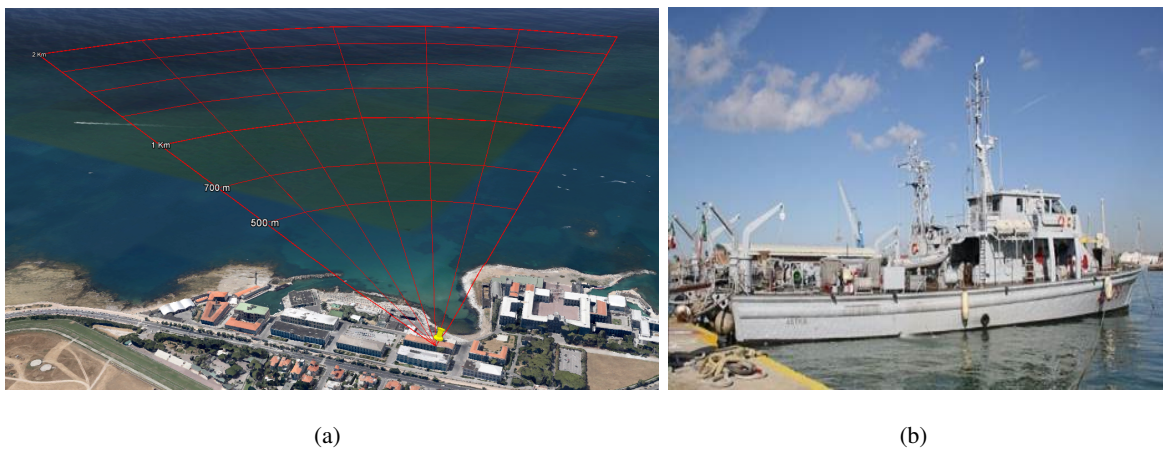
Figure 4. Acquisition scenario: (a) Geometry, (b) Target under test

Target	Astice
Length	33.25 m
Width	6.47 m
Height	12 m

Table III

TARGET SIZE

(a)

(b)

(c)
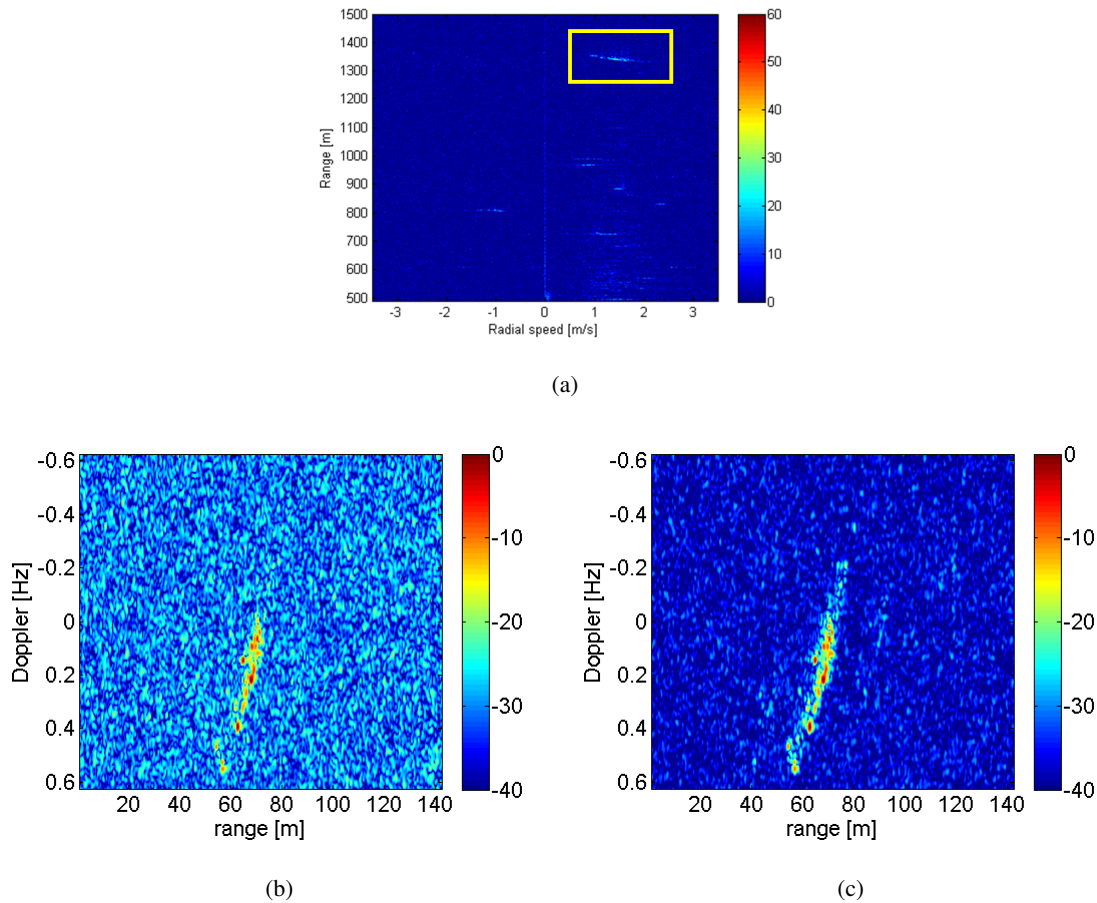
Figure 5. (a) Range-Doppler map with target under test in a yellow box, (b) Target under test (channel C), (c) Target under test (channel V)

B. Performance Analysis

1) 2D reconstruction: The targets can be seen in the range-Doppler map in Fig.5: the target under test is at around 1350 m of distance and has a positive radial speed. A methodology for performance assessment of the 2D image reconstruction based on compressive sensing was proposed in [9]. Specifically, the case of channel C (lower SNR) and the case of channel V/H (higher SNR) will be here analysed for different
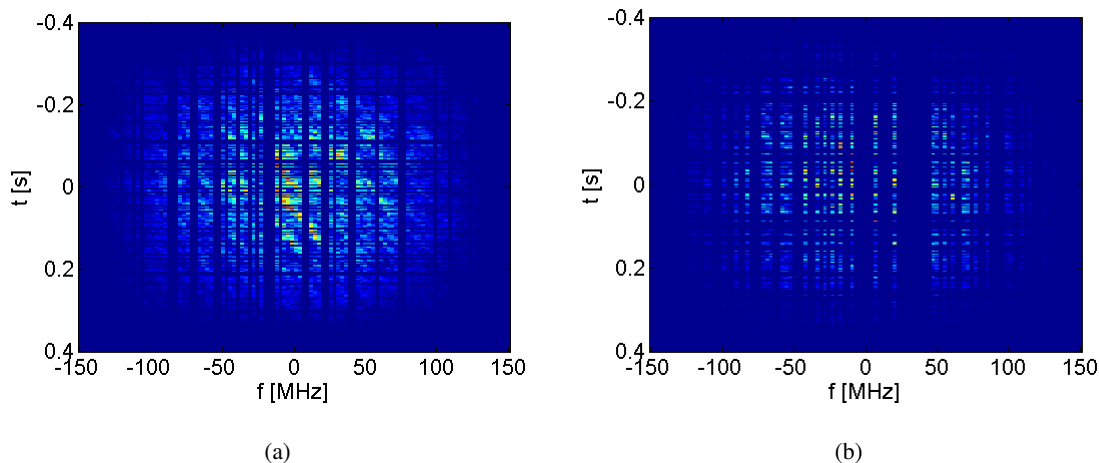
Figure 6. Compressed data: (a) CR=32% (b) CR=64%

values of compression rate (CR). The three reconstruction procedures will be applied and compared. The compressed data with $CR = 32\%$ and $CR = 64\%$ are shown in Fig.6 (a) and (b) respectively. As it can be easily noted the reduction is very evident. The images obtained by applying the conventional Range Doppler (RD) reconstruction to the compressed data are shown in Fig. 7 in which the results obtained with the lower SNR signal (channel C) for two values of compression rate ($CR = 32\%$ and $CR = 64\%$) are shown in Fig. 7 (a) and (b). The same results obtained on the higher SNR signal are instead shown in Fig. 7 (c) and (d).

Fig.8 shows the results obtained by applying the conventional compressed sensing based reconstruction technique. Since the images obtained with the three proposed methods (conventional, global sparsity sum and global sparsity max) are very similar from a visual perspective, the authors decided to show only the ones of the conventional method. By the way, the performance analysis has been carried out for all the methods as it will detailed in the following. Fig.8 (a) and (b) show the reconstructed images obtained with the channel C signal for the two values of compression rate. Fig.8 (c) and (d) show the same results on channel V. As can be noted, the ISAR images are quite well reconstructed and the lower SNR leads to a poorer image quality.

In order to better assess the performance, the amplitude and phase values of the scatterer reconstructed in the right position are reported in Fig.9 and Fig.10 for $CR = 32\%$ and the three different reconstruction techniques applied to the lower and the higher SNR signal respectively.

To assess the performance, the number of correct reconstructed scatterers K_{cr}, the Root Mean Square Error (RMSE) in the amplitude and phase values are shown in Tab.IV and Tab.V for channel C and V
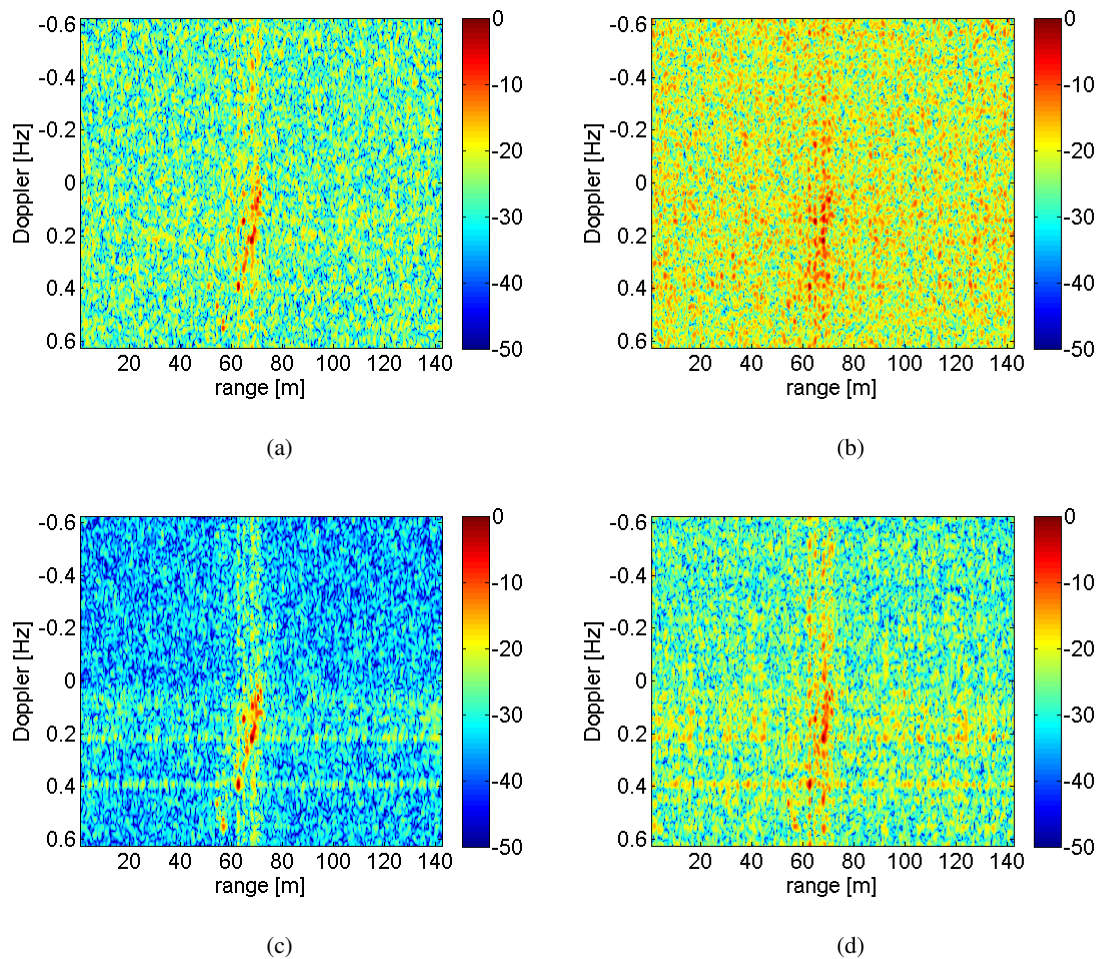
Figure 7. Compressed Image Reconstructed via conventional RD algorithm: (a) Channel C, CR=32% (b) Channel C, CR=64% (c) Channel V, CR=32 (d) Channel V, CR=64%

respectively. The three proposed reconstruction techniques were applied. As can be noted, for higher SNR the three algorithms show more or less the same performance whereas for lower SNR the two global sparsity based reconstruction perform better than the conventional one. The above mentioned results are obtained by averaging on 50 Monte Carlo simulations that is a good balance between accuracy and computational time.

2) 3D reconstruction: Some numerical results are shown in Table VI.

The 3D reconstruction results are shown in Fig.11, Fig.12 and Fig.13. In particular, the comparison of the 3D reconstructions with the Range-Doppler technique (applied to the full data) and with conventional CS with a $CR = 32\%$ and $CR = 64\%$ is shown in Fig.11. The comparison between the different
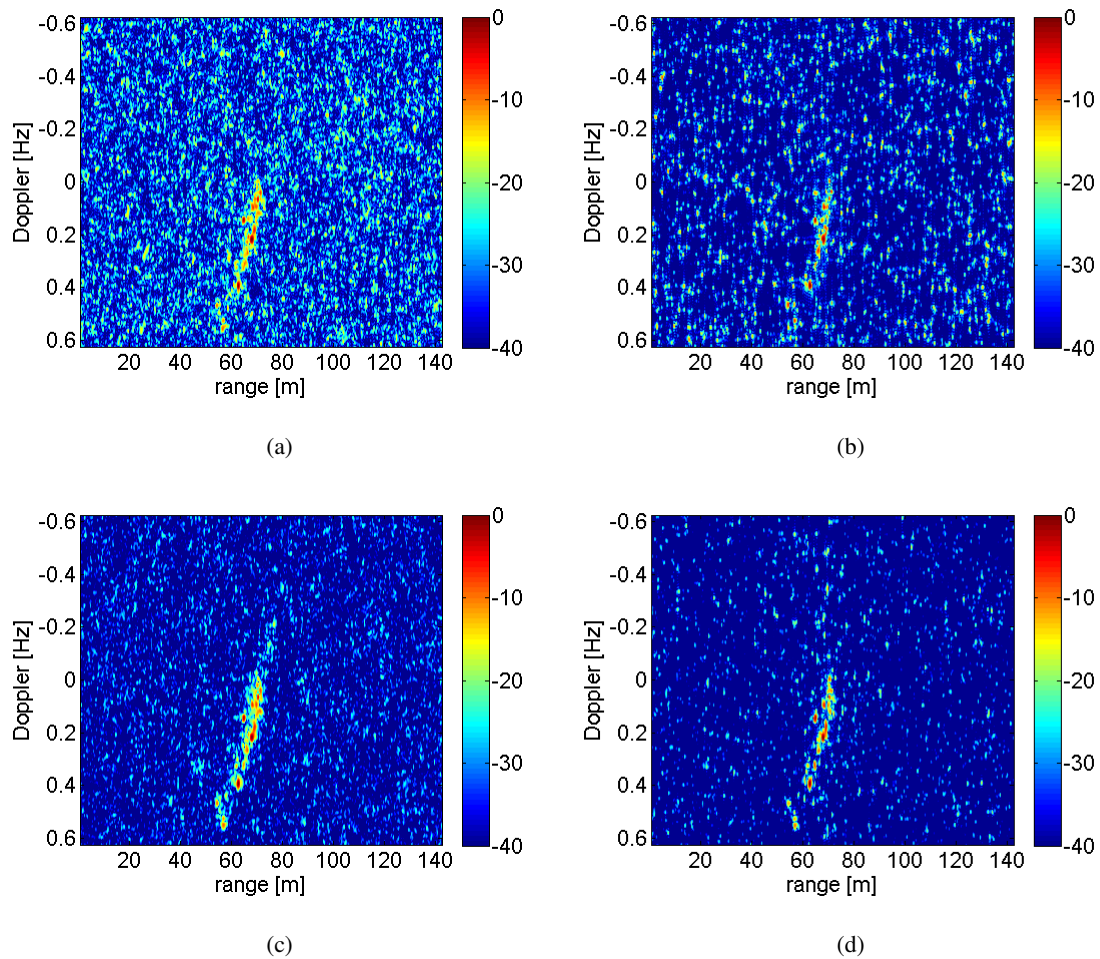
(a)

(b)

(c)

(d)

Figure 8.   Reconstructed Image via conventional CS-based algorithm: (a) Channel C, CR=32% (b) Channel C, CR=64% (c) Channel V, CR=32 (d) Channel V, CR=64%
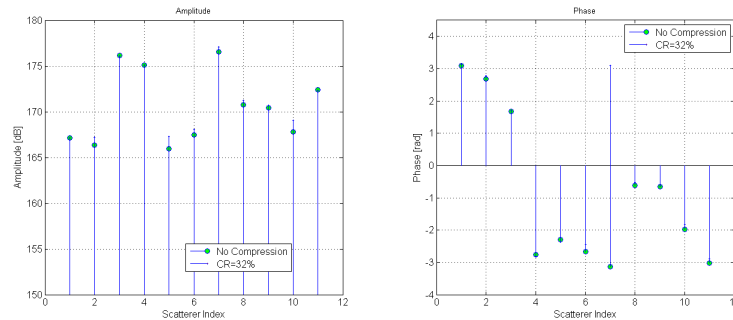
	Conventional			Global Sparsity (sum)			Global Sparsity (max)		
$CR[\%]$	K_{cr}	$RMSE_{amp}\%$	$RMSE_{ph}\%$	K_{cr}	$RMSE_{amp}\%$	$RMSE_{ph}\%$	K_{cr}	$RMSE_{amp}\%$	$RMSE_{ph}\%$
10	15	4.25	5.95	15	3.65	3.02	15	3.95	6.22
32	10	8.22	9.61	10	7.31	7.26	12	7.99	6.51
50	9	14.09	10.9	11	13.06	8.58	11	11.7	8.87
64	6	25.71	15.01	8	15.57	11.43	8	15.68	11.01

Table IV
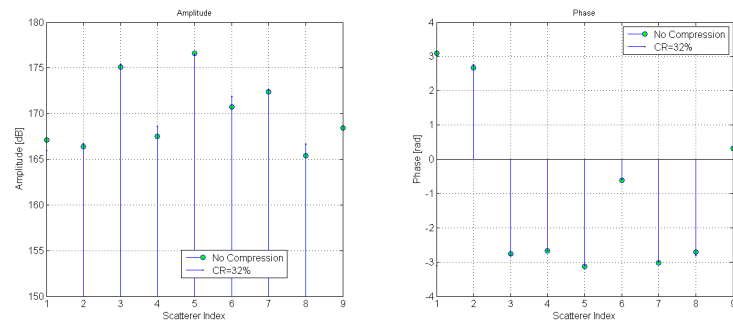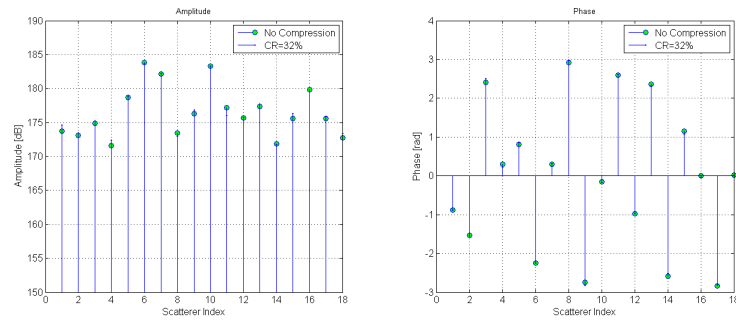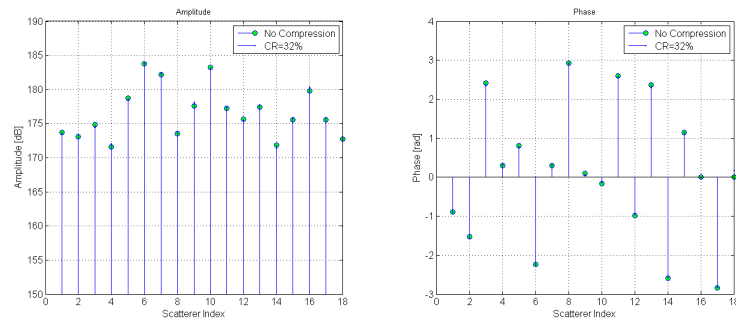
CHANNEL C, PERFORMANCE EVALUATION
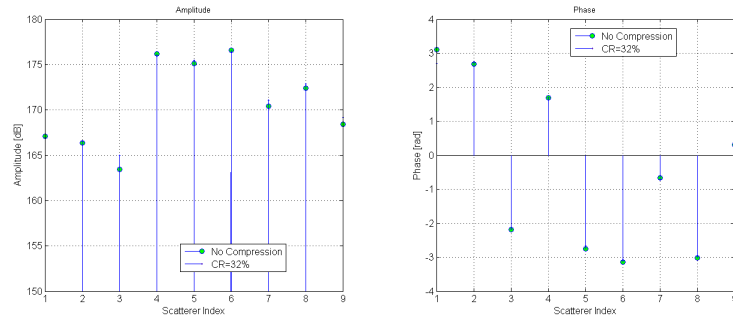
Figure 9. Amplitude and phase values for Channel C, CR=32%: (a) Conventional reconstruction (b) Global Sparsity Sum (c) Global Sparsity max

CS reconstruction techniques, i.e. Conventional, Global sparsity (sum) and Global sparsity (max), are shown in Fig.12 and Fig.13 with a $CR = 32\%$ and $CR = 64\%$, respectively. It should be noted that all the sizes of the target under test match the actual ones except for the length. This is because the MC-CLEAN cannot extract some of the scatterers, in particular the weak scatterers on the bow. This fact underestimates the measure of the vessel's length. A numerical comparison can be performed on the

(a)

(b)
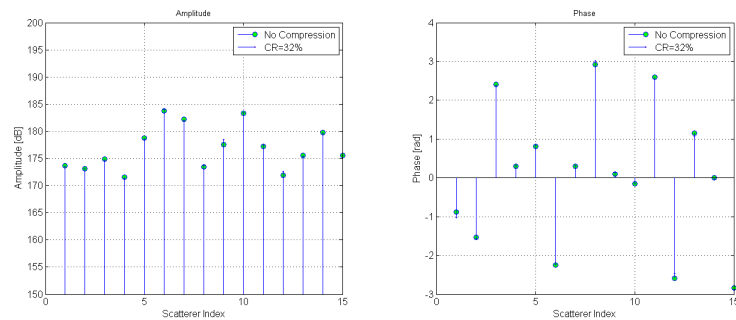
(c)

Figure 10. Amplitude and phase values for Channel V, CR=32%: (a) Conventional reconstruction (b) Global Sparsity Sum (c) Global Sparsity max

estimated effective rotation vector, Ω_{eff}. The RMSE is shown in Fig.14 for different values of CR and different reconstruction procedures. The RMSE on the amplitude and phase value are shown in Fig.14 (a) and (b) respectively. As can be noted global sparsity based reconstruction procedures performs better with respect to the classical one, since they account for the correlation among the channels.

		Conventional			Global Sparsity (sum)			Global Sparsity (max)	
$CR[\%]$	K_{cr}	$RMSE_{amp}\%$	$RMSE_{ph}\%$	K_{cr}	$RMSE_{amp}\%$	$RMSE_{ph}\%$	K_{cr}	$RMSE_{amp}\%$	$RMSE_{ph}\%$
10	19	1.95	6.43	18	1.56	4.35	18	2.01	5.92
32	18	4.21	10.38	18	3.79	7.65	16	3.86	10.24
50	12	6.65	13.79	17	6.99	10.33	18	5.86	9.56
64	12	10.71	14.14	13	11.63	13.53	14	9.62	14.29

Table V

CHANNEL V, PERFORMANCE EVALUATION

Target	Astice
R_0	1324 m
Length	19.4147 m
Height	6.2310 m
Ω_{eff}	0.0452 rad/s
ϕ	43.0559°
v_r	-2.6135 m/s
a_r	0.0206 m/s^2

Table VI

NUMERICAL RESULTS FOR TRIAL WITH PIRAD

IV. CONCLUSION

The applicability of 3D interferometric ISAR reconstruction to ISAR data compressed and reconstructed via Compressive Sensing techniques has been investigated. Specifically, the signal model is derived and then extended in a CS framework. Data acquired during the NATO-Set 196 joint trials are then used to assess the performance of the proposed processing. In details, three sparsity constraints are used for CS reconstruction of 2D ISAR images. It has been proven that global sparsity constraints based reconstruction outperforms conventional one for lower SNR and higher CR. Since 3D image reconstruction relies on the estimation of the effective rotation vector, Ω_{eff} (both amplitude and phase), the estimated values obtained with compressed data are compared with the ones obtained working with the full data. This gives a measure of the goodness of CS based approaches for 3D InISAR application.

REFERENCES

[1] AUSHERMAN, D. A., KOZMA, A., WALKER, J. L., JONES, H. M., AND POGGIO, E. C. Developments in Radar Imaging.

(a) Range-Height plane

(b) Range-Crossrange plane
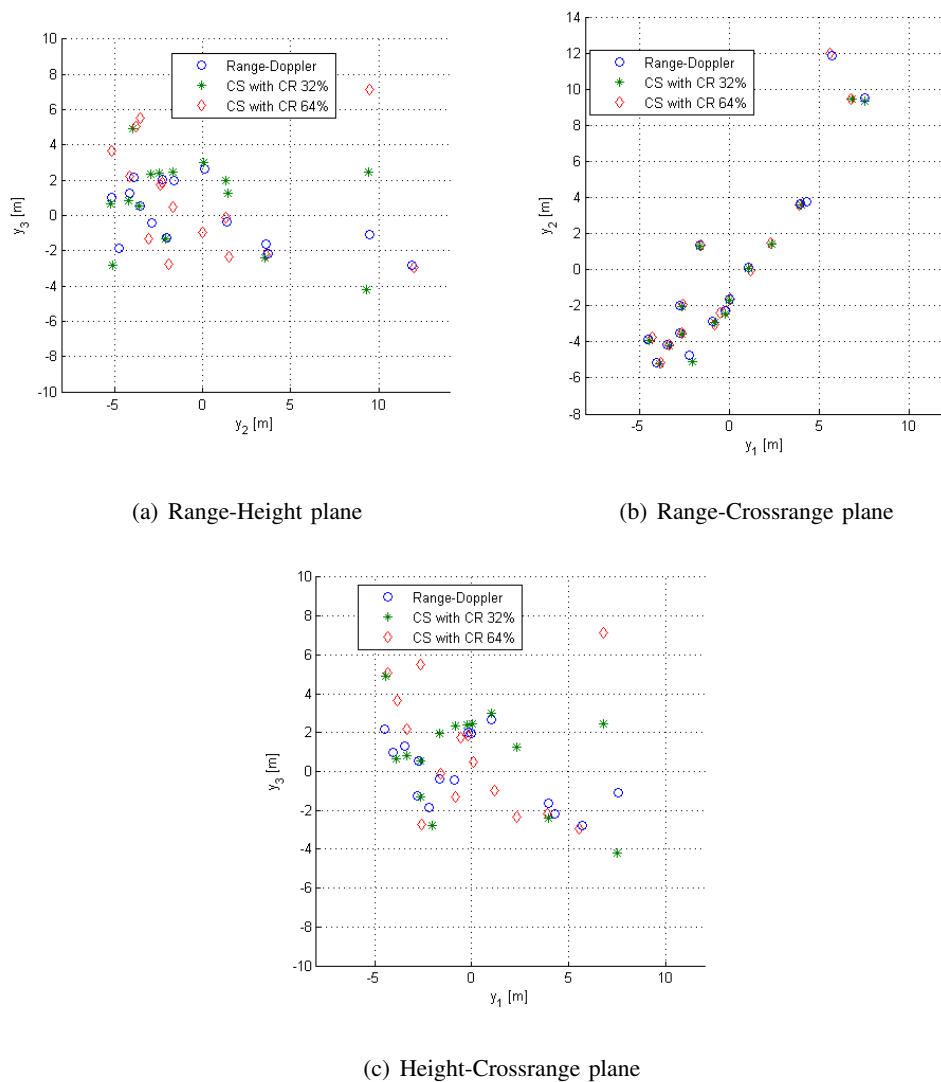

(c) Height-Crossrange plane

Figure 11. 3D reconstruction results with different compression rates

Aerospace and Electronic Systems, IEEE Transactions on AES-20, 4 (July 1984), 363 –400.

[2] BACCI, A., GIUSTI, E., TOMEI, S., MARTORELLA, M., AND BERIZZI, F. Time-slotted FMCW MIMO ISAR with compressive sensing image reconstruction. In *3rd International Workshop on Compressive Sensing applied to Radar (CoSeRa2015)* (Sept 2013).

[3] BARANIUK, R., AND STEEGHS, P. Compressive radar imaging. In *Radar Conference, 2007 IEEE* (April 2007), pp. 128–133.

[4] BERIZZI, F., DALLE MESE, E., DIANI, M., AND MARTORELLA, M. High-resolution ISAR imaging of maneuvering targets by means of the range instantaneous Doppler technique: modeling and performance analysis. *Image Processing, IEEE Transactions on 10*, 12 (Dec 2001), 1880 –1890.

[5] CHINMAY, H., BARANIUK, R., DAVENPORT, M. A., AND DUARTE, M. F. *An Introduction to Compressive Sensing*.

(a) Range-Height plane

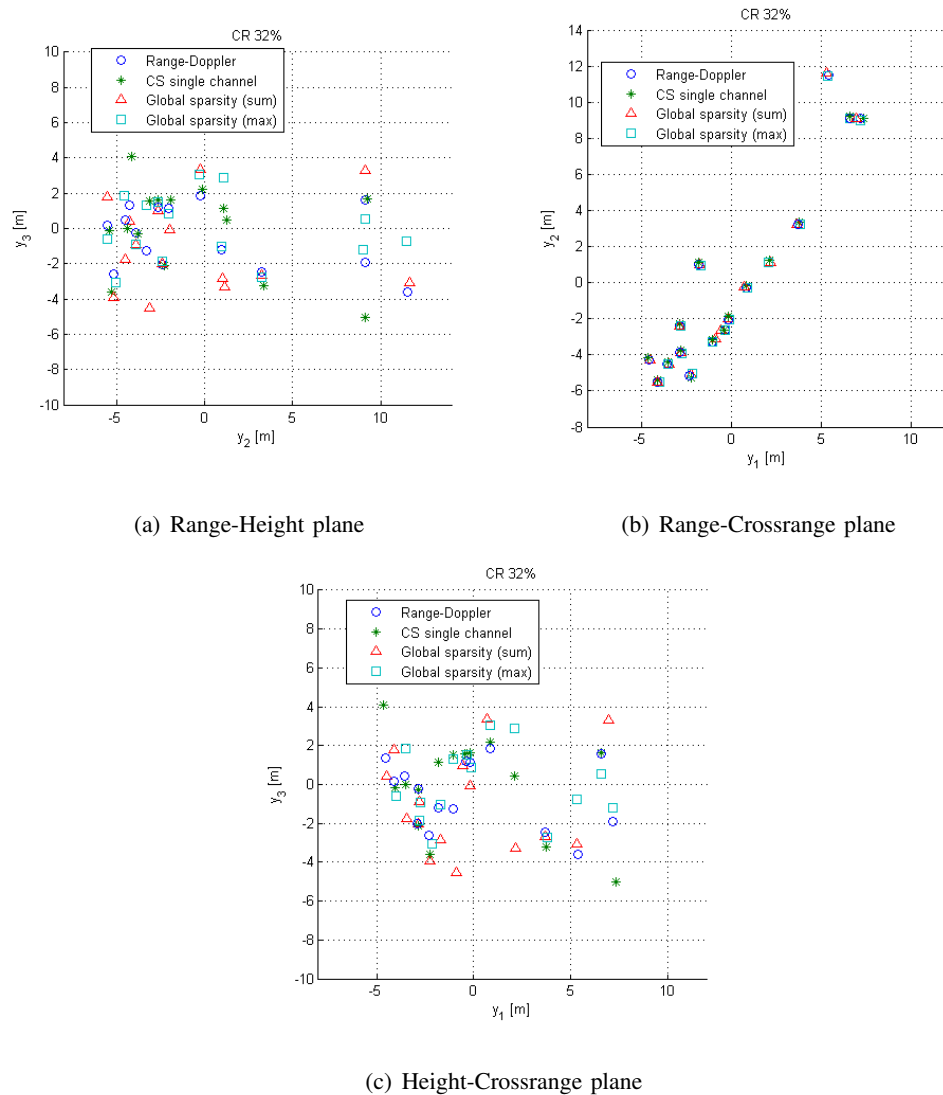
(b) Range-Crossrange plane

(c) Height-Crossrange plane

Figure 12. 3D reconstruction results with different ISAR techniques with a compression rate of 32%

OpenStax CNX., 27 August 2014.

[6] C.Z.MA, T.S.YEO, Q.ZHANG, H.S.TAN, AND J.WANG. Three-dimensional ISAR imaging based on antenna array. *IEEE Transactions on Geoscience and Remote Sensing 46*, 2 (2008), 504–515.

[7] DONOHO, D. Compressed sensing. *Information Theory, IEEE Transactions on 52*, 4 (April 2006), 1289–1306.

[8] GHAFFARI, A., BABAIE-ZADEH, M., AND JUTTEN, C. Sparse decomposition of two dimensional signals. In *Acoustics, Speech and Signal Processing, 2009. ICASSP 2009. IEEE International Conference on* (2009), pp. 3157–3160.

[9] GIUSTI, E., BACCI, A., TOMEI, S., AND MARTORELLA, M. Compressive sensing based ISAR: Performance Evaluation. In *Radar Symposium (IRS), 2015 16th International* (June 2015).

[10] GIVEN, J., AND SCHMIDT, W. Generalized ISAR-part II: interferometric techniques for three-dimensional location of scatterers. *Image Processing, IEEE Transactions on 14*, 11 (Nov. 2005), 1792 –1797.

(a) Range-Height plane
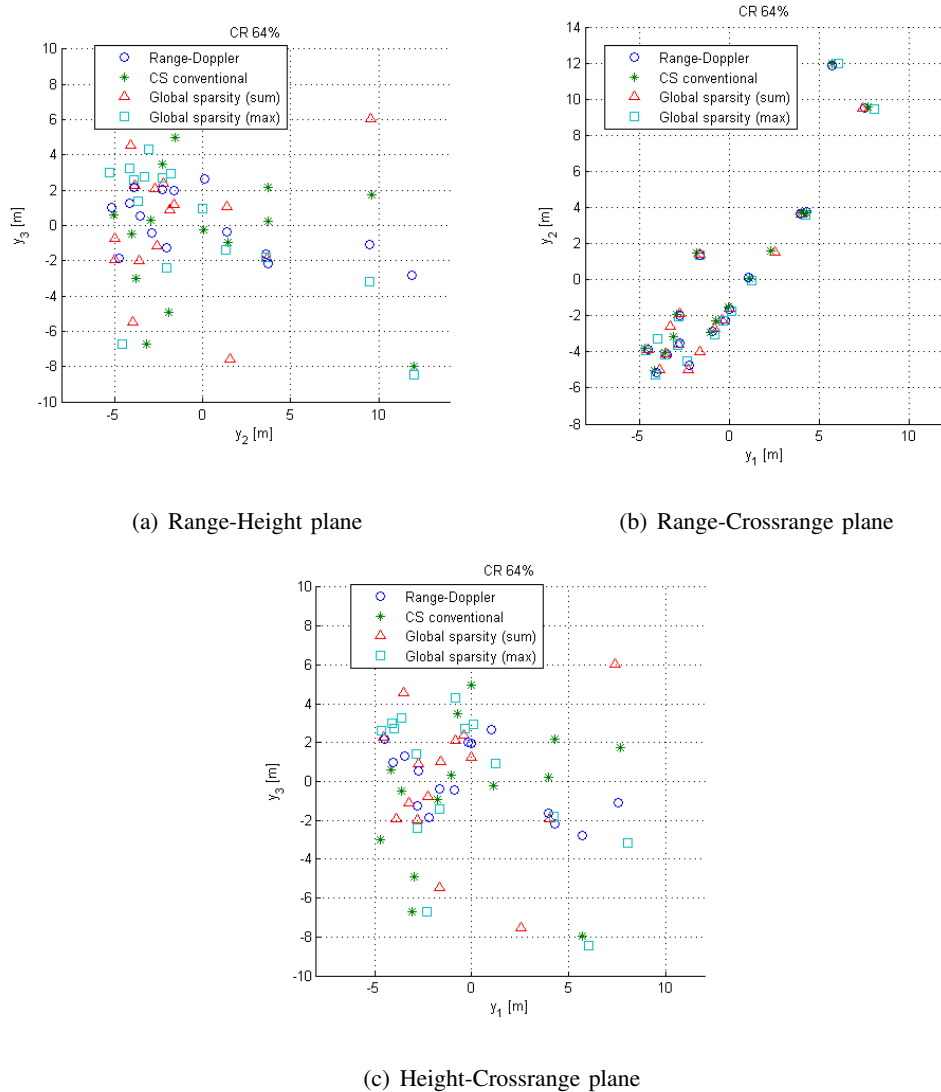
(b) Range-Crossrange plane

(c) Height-Crossrange plane

Figure 13. 3D reconstruction results with different ISAR techniques with a compression rate of 64%

[11] GURBUZ, A. C., McCLELLAN, J., AND SCOTT, W. Compressive sensing for gpr imaging. In *Signals, Systems and Computers, 2007. ACSSC 2007. Conference Record of the Forty-First Asilomar Conference on* (Nov 2007), pp. 2223–2227.

[12] J.A.GIVEN, AND W.R.SCHMIDT. Generalized ISAR - part I: an optimal method for imaging large naval vessels. *IEEE Transactions on Image Processing 14*, 11 (2005), 1783–1791.

[13] J.MAYHAN, M.BURROWS, K.CUOMO, AND J.PIOU. High resolution 3D snapshot ISAR imaging and feature extraction. *IEEE Transactions on Aerospace and Electronic Systems 37*, 2 (2001), 630–642.

[14] K.KNAELL, AND G.CARDILLO. Radar tomography for the generation of three-dimensional images. *IET Proceedings Radar, Sonar and Navigation 142*, 2 (1995), 54–60.

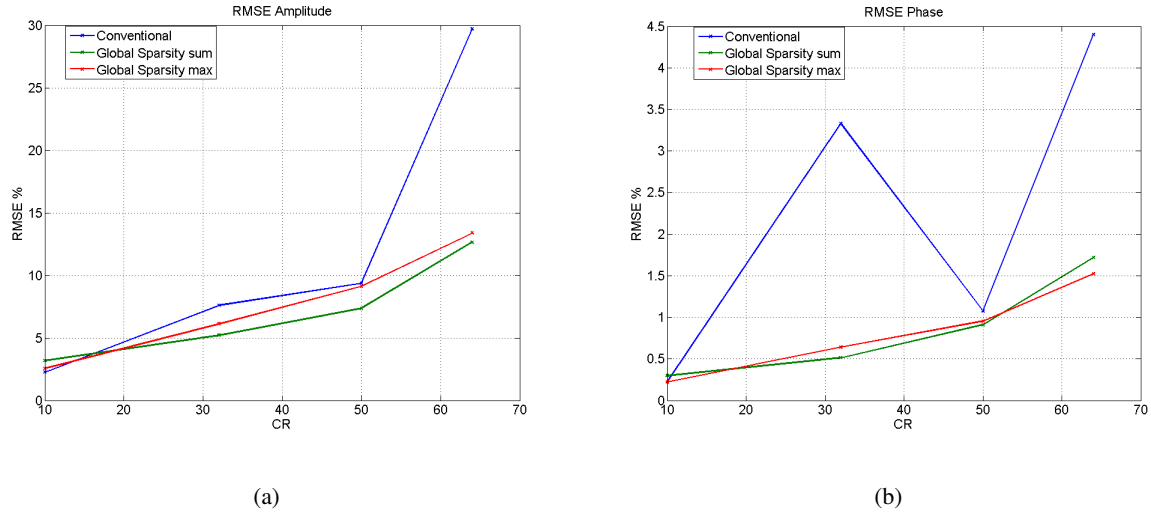[15] K.SUWA, K.YAMAMOTO, M.IWAMOTO, AND T.KIRIMOTO. Reconstruction of 3-D target geometry using radar movie.

Figure 14. RMSE on $\mathbf{\Omega}_{eff}$ estimation: (a) Amplitude, (b) Phase

pp. 1–4.

[16] K.SUWA, T.WAKAYAMA, AND M.IWAMOTO. Three-dimensional target geometry and target motion estimation method using multistatic ISAR movies and its performance. *IEEE Transactions on Geoscience and Remote Sensing 49*, 6 (2011), 2361–2373.

[17] LISCHI, S., MASSINI, R., MUSETTI, L., STAGLIANO, D., BERIZZI, F., NERI, B., AND SAPONARA, S. Low cost FMCW radar design and implementation for harbour surveillance applications. In *International Conference on Electronic Applications, APPLEPIES 2014* (May 2014).

[18] LISCHI, S., MASSINI, R., STAGLIANO, D., MUSETTI, L., BERIZZI, F., NERI, B., AND MARTORELLA, M. X-band compact low cost multi-channel radar prototype for short range high resolution 3D-InISAR. In *European Radar Conference (EuRAD), 2014 11th* (Oct 2014), pp. 157–160.

[19] LUSTIG, M., DONOHO, D., SANTOS, J., AND PAULY, J. Compressed sensing MRI. *Signal Processing Magazine, IEEE 25*, 2 (March 2008), 72–82.

[20] MARTORELLA, M. Introduction to Inverse Synthetic Aperture Radar. In *Elsevier Academic Press Library in Signal Processing: Communications and Radar Signal Processing*. (Vol. 2), 1st Ed., Sept 2013.

[21] MARTORELLA, M., STAGLIANO, D., SALVETTI, F., AND BATTISTI, N. 3D interferometric ISAR imaging of noncooperative targets. *Aerospace and Electronic Systems, IEEE Transactions on 50*, 4 (October 2014), 3102–3114.

[22] QIU, W., GIUSTI, E., BACCI, A., MARTORELLA, M., BERIZZI, F., ZHAO, H., AND FU, Q. Compressive sensing for passive ISAR with DVB-T signal. In *Radar Symposium (IRS), 2013 14th International* (June 2013), vol. 1, pp. 113–118.

[23] QIU, W., MARTORELLA, M., ZHOU, J., ZHAO, H., AND FU, Q. Three-dimensional inverse synthetic aperture radar imaging based on compressive sensing. *Radar, Sonar Navigation, IET 9*, 4 (2015), 411–420.

[24] QIU, W., ZHAO, H., ZHOU, J., AND FU, Q. High-resolution fully polarimetric ISAR imaging based on compressive sensing. *Geoscience and Remote Sensing, IEEE Transactions on 52*, 10 (Oct 2014), 6119–6131.

[25] QIU, W., ZHAO, H., ZHOU, J., AND FU, Q. High-resolution fully polarimetric isar imaging based on compressive sensing. *Geoscience and Remote Sensing, IEEE Transactions on 52*, 10 (Oct 2014), 6119–6131.

[26] STUFF, M., BIANCALANA, M., ARNOLD, G., AND GARBARINO, J. Imaging moving objects in 3D from single aperture Synthetic Aperture Radar. In *Radar Conference, 2004. Proceedings of the IEEE* (April 2004), pp. 94 – 98.

[27] T.KEMPF, M.PEICHL, A. S., AND H.SUESS. 3D tower-turntable ISAR imaging. pp. 114–117.

[28] TOMEI, S. Compressive sensing-based inverse synthetic radar imaging imaging from incomplete data. *IET Radar, Sonar & Navigation* (September 2015).

[29] WALKER, J. Range-Doppler Imaging of Rotating Objects. *Aerospace and Electronic Systems, IEEE Transactions on AES-16*, 1 (Jan. 1980), 23 –52.

[30] WEHNER, D. *High-Resolution Radar*. Artech House Radar Library. Artech House, 1995.

[31] XU, X., AND NARAYANAN, R. Three-dimensional interferometric ISAR imaging for target scattering diagnosis and modeling. *Image Processing, IEEE Transactions on 10*, 7 (Jul 2001), 1094 –1102.

[32] YU, Y., PETROPULU, A., AND POOR, H. Mimo radar using compressive sampling. *Selected Topics in Signal Processing, IEEE Journal of 4*, 1 (Feb 2010), 146–163.

[33] ZHANG, L., QIAO, Z.-J., XING, M., LI, Y., AND BAO, Z. High-resolution ISAR imaging with sparse stepped-frequency waveforms. *Geoscience and Remote Sensing, IEEE Transactions on 49*, 11 (2011), 4630–4651.

[34] ZHANG, L., XING, M., QIU, C.-W., LI, J., AND BAO, Z. Achieving higher resolution ISAR imaging with limited pulses via compressed sampling. *Geoscience and Remote Sensing Letters, IEEE 6*, 3 (2009), 567–571.